

Non-Fermi-liquid scattering rates and anomalous band dispersion in ferropnictides– an ARPES study

J. Fink¹, A. Charnukha^{1,*}, E.D.L. Rienks², Z.H. Liu¹, S. Thirupathaiah^{2,†}, I. Avigo³, F. Roth⁴, H.S. Jeevan^{5,‡},
P. Gegenwart⁵, M. Roslova^{1,6}, I. Morozov^{1,6}, S. Wurmehl^{1,7}, U. Bovensiepen³, S. Borisenko¹, M.
Vojta⁸, B. Büchner^{1,7}

¹*Leibniz Institute for Solid State and Materials Research Dresden, Helmholtzstr. 20, D-01069
Dresden, Germany*

²*Helmholtz-Zentrum Berlin, Albert-Einstein-Strasse 15, D-12489 Berlin, Germany*

³*Fakultät für Physik, Universität Duisburg-Essen, Lotharstr. 1, D-47075 Duisburg, Germany*

⁴*Center for Free-Electron Laser Science / DESY, Notkestrasse 85, D-22607 Hamburg, Germany*

⁵*Institut für Physik, Universität Augsburg, Universitätstr.1, D-86135 Augsburg, Germany*

⁶*Department of Chemistry, Lomonosov Moscow State University, 119991 Moscow, Russia*

⁷*Institut für Festkörperphysik, , Technische Universität Dresden, D-01062 Dresden, Germany*

⁸*Institut für Theoretische Physik , Technische Universität Dresden, D-01062 Dresden, Germany*

December 3, 2024

*Present address: Department of Physics, University of California, San Diego, La Jolla, California 92093, USA

†Present address: Solid State and Structural Chemistry Unit, Indian Institute of Science, Bangalore-560012, India

‡Present address: Department of Physics, PESITM, Sagar Road, 577204 Shimoga, India

Unconventional/high temperature superconductivity (SC) is observed in heavy fermion systems, cuprates, molecular crystals, and ferropnictides close to a point in the phase diagram where, as a function of a control parameter such as pressure, chemical pressure, or doping, the antiferromagnetic order is suppressed^{1,2}. A widespread view is that at this point, which is called a quantum critical point (QCP), strong antiferromagnetic fluctuations are a candidate for the glue mediating superconductivity and that these fluctuations would also account for the normal state non-Fermi-liquid behaviour as is visible in transport and thermal properties. Based on angle-resolved photoemission spectroscopy (ARPES) studies of the band dispersion and the quasiparticle scattering rates in ferropnictides, we propose here a different scenario: a co-action between a highly correlated electron liquid, which can be described by a marginal Fermi liquid³, *and* a crossing of a van Hove singularity, e.g. the top(bottom) of a hole(electron) pocket or a saddle point, through the chemical potential causes an anomalous band dispersion at the Fermi level which leads to a strong mass enhancement in the normal state and to a small effective Fermi energy favoring a Bardeen-Cooper-Schrieffer (BCS)⁴-Bose-Einstein (BE)⁵ crossover state in the superconducting phase. The results can be generalised to other unconventional superconductors.

Introduction

ARPES measures the energy (ω) and momentum (\mathbf{k}) dependent spectral function $A(\omega, \mathbf{k})$ multiplied by a transition matrix element⁶. The former is given by

$$A(\omega, \mathbf{k}) = -\frac{1}{\pi} \frac{\Im \Sigma(\omega, \mathbf{k})}{[\omega - \epsilon_{\mathbf{k}} - \Re \Sigma(\omega, \mathbf{k})]^2 + [\Im \Sigma(\omega, \mathbf{k})]^2}, \quad (1)$$

where $\epsilon_{\mathbf{k}}$ is the bare particle energy, $\Re\Sigma(\omega, \mathbf{k})$ is the real part and $\Im\Sigma(\omega, \mathbf{k})$ is the imaginary part of the self-energy. For small $\Im\Sigma(\omega, \mathbf{k})$ the maxima of the spectral function (the dispersion) are determined by the equation

$$\omega - \epsilon_{\mathbf{k}} - \Re\Sigma(\omega, \mathbf{k}) = 0. \quad (2)$$

In the case when $\Re\Sigma(\omega, \mathbf{k}) = -\lambda\omega$ as in a Fermi liquid close to the chemical potential and when $\Re\Sigma(\omega, \mathbf{k})$ is independent of the momentum, the dispersion follows $\omega = \epsilon_{\mathbf{k}}/(1 + \lambda)$, i.e., with increasing coupling constant λ the maximum of the spectral function is shifted to lower binding energy which means the effective mass is enhanced. In a marginal Fermi liquid, a concept originally devised to phenomenologically describe the normal state of the cuprate superconductors, one assumes that due to strong correlation effects and/or nesting, at low energy the scattering rates are much higher compared to a normal Fermi liquid and the self-energy is given by⁷

$$\Sigma = \frac{1}{2}\lambda_{MF}\omega \ln \frac{\omega_c}{x} - i\frac{\pi}{2}\lambda_{MF}x, \quad (3)$$

where $x = \max(|\omega|, kT)$, kT is the thermal energy, λ_{MF} is a coupling constant, and ω_c is an ultraviolet cutoff energy. In this case $\Re\Sigma$ is no longer linear in energy and one has to solve equation (2) numerically to derive the dispersion.

In a small \mathbf{k} range one can write $\epsilon_{\mathbf{k}} = \epsilon_{\mathbf{k}_0} + (\mathbf{k} - \mathbf{k}_0)\mathbf{v}_{\mathbf{k}}^*$, where $\mathbf{v}_{\mathbf{k}}^* \equiv \nabla \epsilon_{\mathbf{k}}^*|_{\mathbf{k}_0}$ is the renormalized velocity. Replacing $\epsilon_{\mathbf{k}}$ in equation (1) by this k -dependence, at constant energy the momentum distribution curve (MDC) is determined by a Lorentzian with a width W at half height and the lifetime broadening or the inverse scattering rate in the energy scale of the quasiparticles is determined by $\Gamma = \frac{1}{2}Wv_k^*$. If Σ depends weakly on the momentum k the imaginary part of the self-energy

can then be derived from

$$\Im\Sigma = \Gamma \frac{v_k}{v_k^*} = \Gamma \frac{m^*}{m_0}, \quad (4)$$

where v_k is the bare velocity, m_0 is the bare band mass, and m^* is the renormalized mass. Usually v_k is taken from density functional calculations. From this discussion we conclude that ARPES is an ideal tool to study the energy and momentum dependent scattering rate and the mass renormalization close to a QCP.

In this contribution we used ARPES to study the band dispersion, the scattering rate, and the mass enhancement as a function of the control parameter near optimal substitution/doping in the normal state of two ferropnictide⁸ systems: first the compounds $\text{BaFe}_2\text{As}_{2-x}\text{P}_x$ and $\text{EuFe}_2\text{As}_{2-x}\text{P}_x$ (commonly termed 122 compounds), in which As is isovalently substituted by P leading to chemical pressure and second the electron doped compounds $\text{NaFe}_{1-x}\text{Co}_x\text{As}$ and $\text{NaFe}_{1-x}\text{Rh}_x\text{As}$ (commonly termed 111 compounds). All measurements were performed in the paramagnetic or superconducting phase. We have measured along three directions in the Brillouin zone shown in Fig. 1 to reach the high symmetry points on the three hole pockets and on the electron pockets. In this way we also obtain information on sections having different orbital character which are illustrated in Fig. 1 by different colours.

There are numerous ARPES studies on these systems published in the literature^{9–16}. Theoretically a QCP in these systems has been predicted in Refs.^{17,18}. Also from transport and thermal studies of these compounds it was concluded that the observed divergent mass enhancement for a control parameter near the optimal superconducting transition temperature T_c is related

to a QCP^{19,20}, i.e., the mass enhancement would be caused by a coupling of the charge carriers to antiferromagnetic fluctuations.

ARPES on BaFe₂As_{2-x}P_x and EuFe₂As_{2-x}P_x

In Fig. 2a we show an ARPES energy distribution map along cut I of optimally substituted BaFe₂As_{2-x}P_x $x=0.27$ ($T_c = 30$ K) measured close to the $Z = (0, 0, \pi/c)$ point, where c is the lattice constant perpendicular to the FeAs layers. The two inner hole pockets can be clearly resolved. Due to matrix element effects the outer hole pocket is more difficult to see in this system. The data at constant binding energy could be well fitted by four Lorentzians as shown in Fig. 2b for an energy of 80 meV. In this way the renormalized dispersion could be fitted as shown by the red lines in Fig. 2a.

Furthermore, from those fits the life-time broadening, Γ , as a function of the binding energy could be derived for the two hole pockets as presented in Fig. 2c. For both hole pockets, the width increases linearly with binding energy, typical of a marginal Fermi liquid. In a large energy range of $5 \leq \omega \leq 100$ meV, the scattering rates could be fitted by $\Gamma = \alpha + \beta\omega$. The value of α is determined by elastic scattering from impurities at the surface and in the bulk. The coefficient β is determined by inelastic scattering processes. β is much larger for the inner hole pocket compared to the value of the middle hole pocket. Similar results have been presented previously for the system Ba(Fe_{1-x}Co_x)₂As₂²¹.

In the highly correlated systems inelastic scattering processes, described by β , are determined

by intra and inter-band transitions. Phonon excitations can be probably neglected since in the energy dependence of $\Im\Sigma$ no kinks have been detected within the phonon energy range of ≈ 35 meV. The difference in the scattering rates of the two pockets have been predicted by theoretical calculations^{22,23} as the scattering by intra-band transitions should be larger than that by inter-band transitions. In the former the scattering potential is determined by the on-site Coulomb interaction U while in the latter the potential is reduced to $U - J$ where J is the exchange integral. Looking to Fig. 1, one immediately realizes that there is a reasonable nesting between sections on the inner hole pocket having yz orbital character (around point 1) and a section of the electron pocket at M_x (around point 5) having the same orbital character. The same happens when turning the angle by 90° for a nesting of sections of inner hole pocket having xz orbital character with similar sections of the electron pocket at M_y . The middle hole pocket on the other hand shows reasonable nesting conditions only between sections having different orbital character which explains the reduced scattering rate. It is remarkable that the "cold" (middle) hole pocket also shows a marginal Fermi liquid behaviour, although the scattering rate is much lower. This is different from recent ARPES results on cuprates where a more marginal Fermi liquid behaviour was found at the "hot" spots while a Fermi liquid behaviour is realized at the "cold" spots²⁴.

In addition we have performed similar experiments along cut II (not shown). Within error bars we could not find any difference of the scattering rates when compared to those derived along cut I. Furthermore we have investigated in detail the k_z dependence of Γ for cut I and II and within error bars we could not notice any variation. We have done similar experiments on the electron pockets with measurements along cut III and with an extended cut I using higher photon energies.

Details of these results will be published in a forthcoming paper.

In Fig. 2d we present a compilation of all available data of β for $\text{BaFe}_2\text{As}_{2-x}\text{P}_x$ and $\text{EuFe}_2\text{As}_{2-x}\text{P}_x$ taken with photon energies corresponding to $k_z = 0$. A similar compilation for measurements with $k_z = \pi/c$ (not shown) indicates no principal difference to the data presented in Fig. 2d. The data can be summarized in the following way: most of the sections show a scattering rate $\beta \approx 0.75$. Exceptions are the middle hole pocket already discussed above and the outer hole pocket having xy orbital character. This was theoretically predicted²³ and explained by a small phase space for nesting with the small xy sections on the electron pocket. Why the latter sections have a rather high scattering rate is at present not clear.

In Fig. 2e we show the top of the middle and the inner hole pocket as derived from a parabolic fit to the dispersion which was obtained from a fit to the MDC curves (see above). In the unsubstituted samples a splitting between xz and the yz states of the order of 50 meV is observed in the tetragonal paramagnetic phase which is not expected since at the Γ point these bands should be degenerate. On the other hand, a similar splitting has been observed^{25,26} above the structural transition slightly above the Néel temperature in ARPES experiments on detwinned crystals. This splitting was explained in terms of nematic fluctuations which exist above the Néel and the structural transition. As expected from other studies²⁶ in which a decrease of the nematic fluctuations with increasing control parameter has been detected, in the present ARPES experiments the splitting is reduced with increasing control parameter, as well, and disappears near optimal doping where the top of the two hole pockets moves through the chemical potential. On the other hand,

at the Z point the top of the hole pockets move to lower (negative) binding energies leading to an increase of the Fermi wave vector. This development of the hole cylinders and relatively small changes of the electron cylinders as a function of the control parameter is a consequence of the expected charge neutrality upon substitution of As with isovalent P atoms. Thus we have a Lifshitz transition of a Fermi cylinder at low P concentrations to an ellipsoid around the Z point at higher P concentrations. This Lifshitz transitions close to optimal doping/substitution has been detected in 122 systems in several ARPES studies^{10,27–30}.

Finally, at the end of this section, we remark that in the present ARPES study, within error bars, we have not found any major differences in the electronic structure between $\text{BaFe}_2\text{As}_{2-x}\text{P}_x$ and $\text{EuFe}_2\text{As}_{2-x}\text{P}_x$.

ARPES on $\text{NaFe}_{1-x}\text{Co}_x\text{As}$ and $\text{NaFe}_{1-x}\text{Rh}_x\text{As}$

The 111 compounds are ideal for ARPES experiments since they do not form a polar surface after cleaving. Therefore, in the ARPES experiments on 111 compounds one is certain to find bulk properties³¹. On the other hand, they have the disadvantage that close to the Fermi level the middle hole pocket hybridises with the inner hole pocket. As a consequence, reliable results on the scattering rates can be only derived at higher binding energies. In Fig. 3a we show an ARPES energy distribution map of $\text{NaFe}_{1-x}\text{Rh}_x\text{As}$ $x=0.027$ ($T_c = 20$ K) close to the Γ point along cut I. All three hole pockets can be clearly resolved. The data at constant binding energy of 40 meV could be well fitted by six Lorentzians as shown in Fig. 2b. In this way the renormalized dispersion

could be fitted as shown by the red lines in Fig. 3a.

Furthermore, for this compound we derived the life-time broadening Γ as a function of the binding energy for the three hole pockets as presented in Fig. 3c. Again for all three hole pockets, the spectral width in the range where there is no band overlapping increases linearly with binding energy. The highest β value (0.59) is obtained for the inner hole pocket. For the middle hole pocket $\beta = 0.27$ is derived. Finally for the outer hole pocket we obtain a value $\beta = 0.2$. It is interesting to note that ARPES experiments on an other 111 compound (LiFeAs) show the largest superconducting gap for the inner hole pockets (the one having the largest scattering rate), while for the outer hole pocket (having a smaller β value compared to the inner hole pocket) a factor of two smaller energy gap has been detected^{32,33}. This could indicate that the scattering rates are directly related to the formation of the superconducting gap.

We have performed a similar analysis of the ARPES data taken along cut III reaching the point 5 (see Fig. 1). In Fig. 3d we show the corresponding energy distribution map. Fig. 3e depicts the momentum distribution curve together with a fit to two Lorentzians. In Fig. 3f we present the derived scattering rate as a function of binding energy together with a linear fit, yielding a value $\beta = 0.85$. In Fig. 3g we present a compilation of all β values for $\text{NaFe}_{1-x}\text{Co}_x\text{As}$ as a function of Co concentration. As in the case of the 122 compounds, the β values are rather independent of the control parameter and no divergence at optimal doping ($x = 0.027$) is observed. We note here that similar to the case of $\text{BaFe}_2\text{As}_{2-x}\text{P}_x$, discussed above, we observe similar scattering rates at $k_z = \pi/c$ (not shown). Finally, in Fig. 3h the top of the hole pockets as a function of the Co

concentration is depicted. As in the case of the 122 compounds, the crossing of the top of the inner hole pocket, having the strongest scattering rate, occurs very close to optimal doping.

Discussion and model calculations

In Table 1 we list the β values for optimally doped/substituted $\text{BaFe}_2\text{As}_{2-x}\text{P}_x$, $\text{NaFe}_{1-x}\text{Co}_x\text{As}$, and $\text{NaFe}_{1-x}\text{Rh}_x\text{As}$ samples. Assuming a marginal Fermi liquid behavior and using equations (3) and (4) we have calculated the coupling constants, λ_{MF} , from the relation $\lambda_{MF} = \beta \frac{2}{\pi} \frac{m^*}{m_0}$. The bare electron masses m_0 were derived from a parabolic fit to the density functional theory (DFT) calculations for the undoped/unsubstituted compounds^{34,35}, the renormalized masses m^* were evaluated from a parabolic fit of the measured dispersion. Note that these $\frac{m^*}{m_0}$ values are not related to the mass renormalization at the Fermi level. They are needed for the evaluation of λ_{MF} from the β values. From this compilation one realizes large differences in the scattering rates between the three hole pockets in $\text{BaFe}_2\text{As}_{2-x}\text{P}_x$ and a reduction of the differences when going to $\text{NaFe}_{1-x}\text{Co}_x\text{As}$ and finally to $\text{NaFe}_{1-x}\text{Rh}_x\text{As}$. This evolution can be explained by the strength of the scattering potential of the substituents, being weak for the isovalent replacement of As by P, which is outside of the Fe layers, being stronger when Fe is replaced by Co, which occurs inside the Fe layer, and being strongest for replacement of Fe by the heavy element Rh.

The observed independence of the scattering rates from the control parameter in the energy range 5 to ≈ 100 meV could be related to a scenario in which the scattering rates are mainly related to local properties of the electronic system. On the other hand we cannot exclude that below \approx

5 meV corresponding to 50 K that the scattering rates are no more linear in energy, e.g. they are determined by Fermi liquid properties ($\Gamma \propto \omega^2$). The later case would mean that all the present ARPES data would be obtained in the strange metal range were scattering rates linear in energy are expected^{1,2}.

In the following we make first the assumption that we can extrapolate the linear energy dependence of Γ , observed in the ARPES experiments, to zero energy and study the consequences of such a marginal Fermi liquid model. In a second step we perform analogous calculations in which the marginal Fermi liquid behaviour observed above 5 meV is extended by a Fermi liquid behaviour ($\Gamma \propto \omega^2$) below 5 meV.

Assuming a marginal Fermi-liquid behaviour in the full energy range for the imaginary part of the self-energy implies that we should use for the real part of the self-energy the relation given in equation (3) since the imaginary and the real part are connected by the Kramers-Kronig relation. In Fig. 4a we show an energy distribution map of $\text{BaFe}_2\text{As}_{2-x}\text{P}_x$ $x = 0.24$ measured near Γ along cut I using a vertical polarisation. Due to matrix element effects we only see the inner hole pocket. Using an MDC fit we derived the dispersion. This dispersion could be fitted (red line) using both a parabolic bare particle dispersion (black line) derived from DFT calculations and the real part of the marginal Fermi liquid self-energy given by equation (3). Choosing a cut-of energy $\omega_c = 1.5$ eV we obtain a $\lambda_{MF} = 1.46$ which is close to the value derived from the scattering rate. We remark here that in the fits the parameters λ_{MF} and ω_c are strongly correlated. An increase of ω_c to a value of 4 eV reduces λ_{MF} by a factor of two. Analogous data for $\text{NaFe}_{1-x}\text{Rh}_x\text{As}$ are shown in

Fig. 4b. Here we have fitted the dispersion of the outer band (red line) with a marginal Fermi liquid self-energy. The derived coupling constant $\lambda = 1.2$ is close to that obtained from the scattering rate. In Fig. 4a and b we obtain a dispersion which at the Fermi level is strongly reduced compared to the bare particle dispersion depicted by a black line. We emphasise that the weak dispersion near the Fermi level in $\text{NaFe}_{1-x}\text{Rh}_x\text{As}$ is not caused by a coherence peak in the superconducting state since the measurement presented in Fig. 4 b was performed in the normal state at $T = 26$ K.

Based on the marginal Fermi liquid self-energy, we can now calculate the renormalized dispersion close to the Fermi level as a function of the band position. We used the parameters typical of the inner hole pocket of $\text{BaFe}_2\text{As}_{2-x}\text{P}_x$: $\lambda_{MF} = 1.42$, $\omega_c = 1.5$ eV, and an electron mass in units of the free electron mass $m_0 = 0.23$ from DFT calculations on the inner hole pocket of $\text{BaFe}_2\text{As}_{2-x}\text{P}_x$ ³⁴. In Fig. 4d we show such calculations for a hole pocket touching the chemical potential (Fermi energy $E_F = 0$ for the hole pocket), for the bare particle band (black), for $\Re\Sigma$ (green), and for the renormalised band (red). Due to the fact that $\Re\Sigma$ scales to zero logarithmically and is very close to the bare particle dispersion, there is a strong renormalisation close to the Fermi level which leads to a very weakly dispersive band covering a large part of the Brillouin zone. The extension of this singularity increases with increasing λ_{MF} and increasing m_0 . The flat band occurs on an energy scale of about 10 meV. In this energy range, one realizes a mass enhancement which diverges at zero energy. This can be clearly seen in the blue curve showing the second derivative of the renormalized dispersion which determines the effective mass. For comparison we show a $m^*/m_0 = 1$ line (thin dashed blue). In Fig. 4c we depict an analogous calculation but with the top of the bare hole pocket shifted 50 meV above the Fermi level ($E_F = 50\text{meV}$ for the hole pocket).

The calculated renormalised dispersion shows a Fermi energy which at the Γ point is reduced by a factor of four. One immediately realizes that the extension of the weakly renormalized dispersion (red line) is strongly reduced at the Fermi level. Moreover, the divergence of the effective mass curve is shifted by $\Delta E \approx 2.5$ meV into the unoccupied states. The calculation yields that this shift ΔE increases almost linearly with E_F . The asymmetry of the renormalized dispersion and the mass enhancement relative to the Fermi level is related to the asymmetry of the slopes of the bare particle dispersion. Compared to the bare particle mass m_0 , below and at the Fermi level there is only a moderate mass enhancement. We emphasise here that although in the marginal Fermi liquid scenario the quasiparticles have very strong low-energy scattering rates, in the case without a van Hove singularity at the Fermi level, there is no divergent mass enhancement. This means that a marginal Fermi liquid behaviour alone cannot describe the strange normal state properties at a specific value of the control parameter. In Fig. 4e we present analogous calculations for a bare particle hole pocket shifted below 50 meV below the Fermi level. The bare particle dispersion is renormalised at the Γ point by a factor ≈ 5 and the mass enhancement in the center of the Brillouin zone is strongly reduced.

In this simple model it is probably even possible to understand the wedge like non-Fermi-liquid (strange metal) region in the temperature-control parameter phase diagram^{1,2}. Exactly for $E_F = 0$, the divergent mass enhancement will be in the range of thermal excitations. On the other hand, for the cases in which the hole pockets are shifted slightly above or below the Fermi level, as depicted in Fig. 4c and e, at low temperatures thermal excitations reach only ranges with small mass enhancement, while at higher temperatures, the maxima in the m^* curve are broadened (not

shown) leading to higher effective masses at the chemical potential and thus to a strange metal behaviour.

These calculations also can explain why in the published ARPES literature on ferropnictides there are so many rather different values presented for the mass renormalization. The reason for this is once that the effective mass strongly depends on the size of the band shift. Furthermore, since, different from a band with a quadratic dispersion, the mass renormalization is energy dependent and occurs essentially in a narrow energy range, experimental values also strongly depend on the energy resolution and details of the data analysis.

In a second step, we extended the linear ARPES $\Im\Sigma$ by a quadratic energy dependence (Fermi liquid behaviour) below $\omega_0 = 5$ meV (the lower energy border in our ARPES results). The result for $E_F = 0$, which is rather independent of the strength of the scattering rate of the Fermi liquid part, is presented in Fig. 4f. Comparing Fig. 4d and f, there is still a weakly dispersing band at the Fermi level but the divergence of the effective mass at the Γ point is now no more divergent and reduced to $m^*/m_0 \approx 7$. The strong mass enhancement now appears at ω_0 since at this energy we have a discontinuity in $\Im\Sigma$. Analogous calculations for the hole pocket shifted by -50 meV (not shown) yield again that when the van Hove singularity of the hole pocket is not at the Fermi level, the range of the weakly dispersing band is strongly reduced (the renormalised dispersion is very close to that presented in Fig. 4c) and the mass renormalisation at the chemical potential is reduced to ≈ 4 .

These calculations show that in both cases, the linear or the quadratic extension at low ener-

gies of the measured ARPES $\Im\Sigma$, the crossing of a van Hove singularity (in the present calculations the top of the hole pocket) plays an important role for the electronic structure of these correlated systems. It can explain the appearance of control parameter dependent (band shift dependent) mass enhancement. Possibly the divergent mass enhancement in the transport properties observed in $\text{BaFe}_2\text{As}_{2-x}\text{P}_x$ near optimal substitution¹⁹ or the strange behaviour of the thermal properties of $\text{Ba}(\text{Fe}_{1-x}\text{Co}_x)_2\text{As}_2$ ²⁰ can be explained in this model.

Our experimental results can be compared with those from theoretical calculations in the framework of density-functional theory combined with dynamical mean-field theory (DMFT). Interestingly, non-Fermi-liquid-like self-energies have been reported^{36,37} which could be fitted by sublinear power laws over a range of elevated energies. Although the detailed interpretation differs between the two references, this incoherent-metal behavior has been attributed to an interplay of Hubbard and Hund's-rule couplings in a multi-band system: there is a sizable regime where carriers strongly scatter off slowly fluctuating unquenched spins. Importantly, this source of scattering is essentially local in space, implying that it is weakly influenced by longer-range spin correlations and can thus persist over an extended part of the phase diagram. We believe that our observation of a strong, weakly doping-dependent, and approximately energy-linear single-particle scattering rate is consistent with originating from local correlation physics as the one described by DMFT. We point out, however, that the doping dependence of the scattering rate as reported in Ref.³⁶, where non-Fermi-liquid behavior has been seen only for hole but not for electron doping, appears inconsistent with our results.

The discussion of the importance of weakly dispersing bands at the Fermi level dates back to the explanation of high- T_c superconductivity in alloys with A15 structure (e.g. V_3Si) by a peaked $N(\epsilon_F)$ caused by a quasi-one-dimensional single particle electronic structure³⁸. Later on, a correlation of the transition temperatures with Fermi temperatures, derived from magnetic-field penetration depth measurements, showed that in particular the unconventional superconductors have a Fermi energy close to the pair binding energy³⁹. This indicates that in the high- T_c superconductors a breakdown of the Migdal theorem⁴⁰ occurs which was the basis of the standard BCS theory of superconductivity⁴ and which requires the inclusion of non-adiabatic effects and the generalisation of the Eliashberg equations⁴¹ and which interpolates between the BCS theory and the Bose-Einstein condensation. Moreover, a recent compilation of the electronic structure of unconventional superconductors⁴² pointed out that most of the high- T_c superconductors have a van Hove singularity at the Fermi level. On the other hand, many of the mentioned compounds fulfill this criteria but have no peaked $N(\epsilon_F)$. For example the optimally doped ferropnictides have a van Hove singularity, i.e. an edge at the chemical potential μ but all DFT calculation predict no peaked bare band density of states at μ in this quasi-two-dimensional electronic structure.

On the other hand there are several ARPES publications on iron-based superconductors which show clear indications of weakly dispersing bands at the Fermi level, which cannot be explained on the basis of DFT calculations, leading to a peaked $N(\epsilon_F)$ and thus to Fermi energies comparable to bosonic excitations. In the ferrochalcogenides an apparently non-dispersive peak at μ has been detected by ARPES which is not in agreement with DFT calculations⁴³. Moreover, in the same system "shallow pockets" have been detected which could lead to a BCS-BE crossover in

the superconducting phase⁴⁴. In addition huge mass renormalisations up to 20 have been reported for ferrochalcogenides⁴⁵ which were explained in terms of a normal renormalization by correlation effects.

Comparison with other unconventional superconductors

Based on transport and thermal properties in hole doped cuprates there is a longstanding discussion on the existence of a QCP near optimal doping at a doping concentration of about 0.2^{7,46}. In particular also in these unconventional superconductors a linear temperature dependence of the resistivity has been observed. ARPES data indicate that at optimal doping, no divergence of the scattering rate along the nodal direction is observed⁴⁷ and that a the saddle point of the two-dimensional electronic structure near $(\pi, 0)$ moves through the Fermi level. In an ARPES study on $\text{YBa}_2\text{Cu}_3\text{O}_{7-\delta}$ an "extended" van Hove singularity has been found⁴⁸ which nicely can be explained by the scenario described above: a co-action between a marginal Fermi liquid behaviour and a weakly dispersing band (the saddle point) moving through the Fermi level.

Similarly, ARPES experiments⁴⁹ on the bilayer ruthenate $\text{Sr}_3\text{Ru}_2\text{O}_7$, which is a sister compound of the triplet superconductor Sr_2RuO_4 , have revealed itinerant Ru $3d$ states confined over large parts of the Brillouin zone to an energy range $< 6 \text{ meV}$, nearly three orders of magnitude lower than the bare band width. The energy scale detected in the ARPES experiments is consistent with that derived for the mass enhancement from thermodynamic measurements.

Finally we mention that also in several heavy-fermion metals quantum critical behaviour

has been found together with a sharp change of the Fermi surface, which has been interpreted as signature of the local destruction of the Kondo singlet formation², i.e., changes of the band dispersion at the Fermi level.

Summary

We have measured the scattering rates of chemically pressurised and of *n*-type doped ferropnictides at various high symmetry points on the hole pockets and the electron pockets. In the range of the investigated control parameter between undoped/non-substituted and slightly over-doped/oversubstituted compounds we realize a linear energy dependence of the scattering rates. Remarkable differences of the strength of the scattering rates on different hole pockets and different sites of the electron pockets are detected which can be explained by the fact that intraband scattering between sections having the same orbital character are stronger than interband scattering between sections having different orbital character. The differences are reduced upon increasing the scattering potential of the doping atoms. As a function of the size of the control parameter we see within error bars no change of the scattering rates for energies larger than 5 meV. In particular, we see no divergence of the scattering rates close to the expected QCP. Furthermore at optimal doping/substitution the edge of the hole pockets having large scattering rates crosses the Fermi level. The strange normal state transport and thermal properties near optimal substitution/doping can be explained by a proposed scenario in which a co-action of the real part of the marginal Fermi liquid self-energy with a van Hove singularity at the Fermi level leads to a weakly dispersing band at the Fermi level and to divergent or strongly enhanced effective masses which can explain the

strange transport and thermal properties in the normal state. The high effective masses imply small effective Fermi energies which could be comparable to bosonic energies mediating superconducting pairing. Thus possible the Migdal's theorem is violated in the unconventional superconductors which could lead to a phase which is near the BCS-BE crossover. The results can be generalised to other unconventional superconductors and possibly are a recipe for future search of new high- T_c superconductors.

Methods

Crystal growth Single crystals of $\text{BaFe}_2\text{As}_{2-x}\text{P}_x$ and $\text{EuFe}_2\text{As}_{2-x}\text{P}_x$ were grown using the FeAs self-flux method⁵⁰. The $\text{NaFe}_{1-x}\text{Co}_x\text{As}$ and $\text{NaFe}_{1-x}\text{Rh}_x\text{As}$ crystals were grown by a self-flux technique⁵¹.

ARPES ARPES measurements were conducted at the 1²- and 1³-ARPES endstations attached to the beamline UE112 PGM 2 at the Berlin Synchrotron (BESSY) with energy and angle resolutions between 4 and 10 meV and 0.2 °, respectively. If not otherwise stated the measuring temperature at the 1²- and 1³-ARPES endstations were 30 and 0.9 K, respectively. Variable photon energies between 30 and 120 eV have been used to change the momentum, k_z , perpendicular to the FeAs layers. Variable photon polarization has been used to change the visibility of the bands having different orbital character.

Acknowledgements This work was financially supported by the German Research Foundation the DFG through the priority program SPP1458.

Author Contributions B.B., U.B., J.F., S.B., and P.G. conceived the research projects on ferropnictides within the priority program. A.C., E.D.L.R., Z.H.L., S.T., I.A., F.R. and J.F. conducted the ARPES experiments. H.S.J. and P.G. grew the $\text{BaFe}_2\text{As}_{2-x}\text{P}_x$ and $\text{EuFe}_2\text{As}_{2-x}\text{P}_x$ single crystals. M.R., I.M., and S.W. grew the $\text{NaFe}_{1-x}\text{Co}_x\text{As}$ and $\text{NaFe}_{1-x}\text{Rh}_x\text{As}$ single crystals. J.F. analyzed the results and developed the concept of combining marginal Fermi liquid theory and flat band dispersion to achieve a divergent mass enhancement. J.F. and E.D.L.R. prepared the manuscript. E.D.L.R., U.B., S.B., M.V., and B.B. contributed with discussions.

Competing Interests The authors declare that they have no competing financial interests.

Correspondence Correspondence and requests for materials should be addressed to J.F. (email: J.Fink@ifw-dresden.de).

1. Löhneysen, H. v., Rosch, A., Vojta, M. & Wölfle, P. Fermi-liquid instabilities at magnetic quantum phase transitions. *Rev. Mod. Phys.* **79**, 1015–1075 (2007). URL <http://link.aps.org/doi/10.1103/RevModPhys.79.1015>.
2. Gegenwart, P., Si, Q. & Steglich, F. Quantum criticality in heavy-fermion metals. *Nat Phys* **4**, 186–197 (2008). URL <http://dx.doi.org/10.1038/nphys892>.
3. Varma, C. M., Littlewood, P. B., Schmitt-Rink, S., Abrahams, E. & Ruckenstein, A. E. Phenomenology of the normal state of Cu – O high-temperature superconductors. *Phys. Rev. Lett.* **63**, 1996–1999 (1989). URL <http://link.aps.org/doi/10.1103/PhysRevLett.63.1996>.

4. Bardeen, J., Cooper, L. N. & Schrieffer, J. R. Theory of Superconductivity. *Physical Review* **108**, 1175–1204 (1957). URL <http://link.aps.org/doi/10.1103/PhysRev.108.1175>.
5. Bose, S. N. Plancks Gesetz und Lichtquantenhypothese. *Z. phys* **26**, 178 (1924).
6. Damascelli, A., Hussain, Z. & Shen, Z.-X. Angle-resolved photoemission studies of the cuprate superconductors. *Rev. Mod. Phys.* **75**, 473–541 (2003). URL <http://link.aps.org/doi/10.1103/RevModPhys.75.473>.
7. Varma, C., Nussinov, Z. & van Saarloos, W. Singular or non-fermi liquids. *Physics Reports* **361**, 267–417 (2002). URL <http://www.sciencedirect.com/science/article/pii/S0370157301000606>.
8. Johnston, D. C. The puzzle of high temperature superconductivity in layered iron pnictides and chalcogenides. *Adv. Phys.* **59**, 803 (2010). URL <http://dx.doi.org/10.1080/00018732.2010.513480>.
9. Shishido, H. *et al.* Evolution of the Fermi surface of $\text{BaFe}_2(\text{As}_{1-x}\text{P}_x)_2$ on entering the superconducting dome. *Phys. Rev. Lett.* **104**, 057008 (2010).
10. Thirupathaiah, S. *et al.* Dissimilarities between the electronic structure of chemically doped and chemically pressurized iron pnictides from an angle-resolved photoemission spectroscopy study. *Phys. Rev. B* **84**, 014531 (2011). URL <http://link.aps.org/doi/10.1103/PhysRevB.84.014531>.

11. Shimojima, T. *et al.* Orbital-independent superconducting gaps in iron pnictides. *Science* **332**, 564–567 (2011). URL <http://www.sciencemag.org/content/332/6029/564.abstract>.
12. He, C. *et al.* Electronic-structure-driven magnetic and structure transitions in superconducting NaFeAs single crystals measured by angle-resolved photoemission spectroscopy. *Phys. Rev. Lett.* **105**, 117002 (2010). URL <http://link.aps.org/doi/10.1103/PhysRevLett.105.117002>.
13. Liu, Z.-H. *et al.* Unconventional superconducting gap in NaFe_{0.95}Co_{0.05}As observed by angle-resolved photoemission spectroscopy. *Phys. Rev. B* **84**, 064519 (2011). URL <http://link.aps.org/doi/10.1103/PhysRevB.84.064519>.
14. Yoshida, T. *et al.* Two-dimensional and three-dimensional Fermi surfaces of superconducting BaFe₂(As_{1-x}P_x)₂ and their nesting properties revealed by angle-resolved photoemission spectroscopy. *Phys. Rev. Lett.* **106**, 117001 (2011). URL <http://link.aps.org/doi/10.1103/PhysRevLett.106.117001>.
15. Thirupathaiah, S. *et al.* Weak-coupling superconductivity in electron-doped NaFe_{0.95}Co_{0.05}As revealed by ARPES. *Phys. Rev. B* **86**, 214508 (2012). URL <http://link.aps.org/doi/10.1103/PhysRevB.86.214508>.
16. Ye, Z. R. *et al.* Orbital selective correlations between nesting/scattering/Lifshitz transition and the superconductivity in AFe_{1-x}Co_xAs (A = Li, Na). *ArXiv e-prints* (2013). URL <http://adsabs.harvard.edu/abs/2013arXiv1303.0682Y>. 1303.0682.

17. Dai, J., Si, Q., Zhu, J.-X. & Abrahams, E. Iron pnictides as a new setting for quantum criticality. *PNAS* **106**, 4118 (2009).
18. Abrahams, E. & Si, Q. Quantum criticality in the iron pnictides and chalcogenides. *Journal of Physics: Condensed Matter* **23**, 223201 (2011). URL <http://stacks.iop.org/0953-8984/23/i=22/a=223201>.
19. Analytis, J. G. *et al.* Transport near a quantum critical point in $\text{BaFe}_2(\text{As}_{1-x}\text{P}_x)_2$. *Nat Phys* **10**, 194–197 (2014). URL <http://dx.doi.org/10.1038/nphys2869>.
20. Meingast, C. *et al.* Thermal expansion and Grüneisen parameters of $\text{Ba}(\text{Fe}_{1-x}\text{Co}_x)_2\text{As}_2$: A thermodynamic quest for quantum criticality. *Phys. Rev. Lett.* **108**, 177004 (2012). URL <http://link.aps.org/doi/10.1103/PhysRevLett.108.177004>.
21. Brouet, V. *et al.* Orbitaly resolved lifetimes in $\text{Ba}(\text{Fe}_{0.92}\text{Co}_{0.08})_2\text{As}_2$ measured by ARPES. *arXiv e-prints:1105.5604* (2011). 1105.5604.
22. Graser, S., Maier, T. A., Hirschfeld, P. J. & Scalapino, D. J. Near-degeneracy of several pairing channels in multiorbital models for the Fe pnictides. *New J. Phys.* **11**, 025016 (2009).
23. Kemper, A. F. *et al.* Anisotropic quasiparticle lifetimes in Fe-based superconductors. *Phys. Rev. B* **83**, 184516 (2011). URL <http://link.aps.org/doi/10.1103/PhysRevB.83.184516>.
24. Rienks, E. *et al.* High-energy anomaly in the angle-resolved photoemission spectra of $\text{Nd}_{2-x}\text{Ce}_x\text{CuO}_4$: Evidence for a matrix element effect. *Phys. Rev. Lett.* **113**, 137001– (2014). URL <http://link.aps.org/doi/10.1103/PhysRevLett.113.137001>.

25. Yi, M. *et al.* Symmetry-breaking orbital anisotropy observed for detwinned $\text{Ba}(\text{Fe}_{1-x}\text{Co}_x)_2\text{As}_2$ above the spin density wave transition. *PNSA* **108**, 6878 (2011).
26. Fisher, I. R., Degiorgi, L. & Shen, Z. X. In-plane electronic anisotropy of underdoped 122 Fe-arsenide superconductors revealed by measurements of detwinned single crystals. *Rep. Progr. Phys.* **74**, 124506 (2011). URL <http://stacks.iop.org/0034-4885/74/i=12/a=124506>.
27. Brouet, V. *et al.* Nesting between hole and electron pockets in $\text{Ba}(\text{Fe}_{1-x}\text{Co}_x)_2\text{As}_2$ ($x = 0-0.3$) observed with angle-resolved photoemission. *Phys. Rev. B* **80**, 165115 (2009).
28. Liu, C. *et al.* Evidence for a Lifshitz transition in electron-doped iron arsenic superconductors at the onset of superconductivity. *Nat Phys* **6**, 419–423 (2010). URL <http://dx.doi.org/10.1038/nphys1656>.
29. Thirupathaiah, S. *et al.* Orbital character variation of the Fermi surface and doping dependent changes of the dimensionality in $\text{BaFe}_{2-x}\text{Co}_x\text{As}_2$ from angle-resolved photoemission spectroscopy. *Phys. Rev. B* **81**, 104512 (2010).
30. Liu, C. *et al.* Importance of the Fermi-surface topology to the superconducting state of the electron-doped pnictide $\text{Ba}(\text{Fe}_{1-x}\text{Co}_x)_2\text{As}_2$. *Phys. Rev. B* **84**, 020509 (2011). URL <http://link.aps.org/doi/10.1103/PhysRevB.84.020509>.
31. Lankau, A. *et al.* Absence of surface states for LiFeAs investigated using density functional calculations. *Phys. Rev. B* **82**, –184518 (2010). URL <http://link.aps.org/doi/10.1103/PhysRevB.82.184518>.

32. Borisenko, S. V. *et al.* One-sign order parameter in iron based superconductor. *Symmetry* **4**, 251–264 (2012).
33. Umezawa, K. *et al.* Unconventional anisotropic s-wave superconducting gaps of the LiFeAs iron-pnictide superconductor. *Phys. Rev. Lett.* **108**, 037002 (2012). URL <http://link.aps.org/doi/10.1103/PhysRevLett.108.037002>.
34. Singh, D. J. Electronic structure and doping in BaFe₂As₂ and LiFeAs: Density functional calculations. *Phys. Rev. B* **78**, 094511 (2008).
35. Deng, S., Köhler, J. & Simon, A. Electronic structure and lattice dynamics of NaFeAs. *Phys. Rev. B* **80**, 214508 (2009). URL <http://link.aps.org/doi/10.1103/PhysRevB.80.214508>.
36. Werner, P. *et al.* Satellites and large doping and temperature dependence of electronic properties in hole-doped BaFe₂As₂. *Nat Phys* **8**, 331–337 (2012). URL <http://dx.doi.org/10.1038/nphys2250>.
37. Yin, Z. P., Haule, K. & Kotliar, G. Fractional power-law behavior and its origin in iron-chalcogenide and ruthenate superconductors: Insights from first-principles calculations. *Phys. Rev. B* **86**, 195141– (2012). URL <http://link.aps.org/doi/10.1103/PhysRevB.86.195141>.
38. Labbe, J. & Friedel, J. Instabilite electronique et changement de phase cristalline des composes du type V₃Si a basse temperature. *J. Phys. France* **27**, 153–165 (1966). URL <http://dx.doi.org/10.1051/jphys:01966002703-4015300>.

39. Uemura, Y. J. *et al.* Basic similarities among cuprate, bismuthate, organic, chevre-phase, and heavy-fermion superconductors shown by penetration-depth measurements. *Phys. Rev. Lett.* **66**, 2665–2668 (1991). URL <http://link.aps.org/doi/10.1103/PhysRevLett.66.2665>.
40. Migdal, A. B. Interaction between electrons and lattice vibrations in a normal metal. *Soviet Physics JETP – USSR* **7**, 996–1001 (1958).
41. Grimaldi, C., Pietronero, L. & Strässler, S. Nonadiabatic superconductivity: Electron-phonon interaction beyond Migdal's theorem. *Phys. Rev. Lett.* **75**, 1158–1161 (1995). URL <http://link.aps.org/doi/10.1103/PhysRevLett.75.1158>.
42. Borisenko, S. Superconductivity: Fewer atoms, more information. *Nat Mater* **12**, 600–601 (2013). URL <http://dx.doi.org/10.1038/nmat3683>.
43. Starowicz, P. *et al.* A flat band at the chemical potential of a $\text{Fe}_{1.03}\text{Te}_{0.94}\text{S}_{0.06}$ superconductor observed by angle-resolved photoemission spectroscopy. *Journal of Physics: Condensed Matter* **25**, 195701 (2013). URL <http://stacks.iop.org/0953-8984/25/i=19/a=195701>.
44. Lubashevsky, Y., Lahoud, E., Chashka, K., Podolsky, D. & Kanigel, A. Shallow pockets and very strong coupling superconductivity in $\text{FeSe}_x\text{Te}_{1-x}$. *Nat Phys* **8**, 309–312 (2012). URL <http://dx.doi.org/10.1038/nphys2216>.
45. Tamai, A. *et al.* Strong electron correlations in the normal state of the iron-based $\text{FeSe}_{0.42}\text{Te}_{0.58}$ superconductor observed by angle-resolved photoemission spectroscopy. *Phys. Rev. Lett.* **104**,

- 097002 (2010). URL <http://link.aps.org/doi/10.1103/PhysRevLett.104.097002>.
46. Tallon, J. & Loram, J. The doping dependence of T^* what is the real high- T_c phase diagram? *Physica C: Superconductivity* **349**, 53–68 (2001). URL <http://www.sciencedirect.com/science/article/pii/S0921453400015240>.
47. Kordyuk, A. A. *et al.* Constituents of the quasiparticle spectrum along the nodal direction of high- T_c cuprates. *Phys. Rev. Lett.* **97**, 017002– (2006). URL <http://link.aps.org/doi/10.1103/PhysRevLett.97.017002>.
48. Gofron, K. *et al.* Observation of an "extended" van Hove singularity in $\text{YBa}_2\text{Cu}_4\text{O}_8$ by ultrahigh energy resolution angle-resolved photoemission. *Phys. Rev. Lett.* **73**, 3302–3305 (1994). URL <http://link.aps.org/doi/10.1103/PhysRevLett.73.3302>.
49. Allan, M. P. *et al.* Formation of heavy d-electron quasiparticles in $\text{Sr}_3\text{Ru}_2\text{O}_7$. *New Journal of Physics* **15**, 063029 (2013). URL <http://stacks.iop.org/1367-2630/15/i=6/a=063029>.
50. Jeevan, H. S., Kasinathan, D., Rosner, H. & Gegenwart, P. Interplay of antiferromagnetism, ferromagnetism, and superconductivity in $\text{EuFe}_2(\text{As}_{1-x}\text{P}_x)_2$ single crystals. *Phys. Rev. B* **83**, 054511 (2011). URL <http://link.aps.org/doi/10.1103/PhysRevB.83.054511>.

51. Steckel, F. *et al.* Characterization of doped $\text{NaFe}_{1-x}\text{T}_x\text{As}$ single crystals with $\text{T} = \text{Pd}, \text{Ni}, \text{Cr}, \text{and Mn}$. *J. Superconduc. Novel Mag.* **1**, 1557–1939 (2014). URL <http://dx.doi.org/10.1007/s10948-014-2748-0>.

Table 1, Ratios of the renormalized mass m^* (derived from a parabolic fit of the ARPES dispersion) to the bare particle mass m_0 (derived from DFT calculations). These ratios were used to calculate the coupling constants λ_{MF} for optimally doped/substituted samples from the β values using equation (4).

Point	BaFe ₂ As _{2-x} P _x	NaFe _{1-x} Co _x As	NaFe _{1-x} Rh _x As
	m^*/m_0	m^*/m_0	m^*/m_0
1	3.1	10.0	10.0
2	6.4	10.0	10.0
7	5.8	11.5	11.5
5	-	-	-
6	-	-	-
	β λ_{MF}	β λ_{MF}	β λ_{MF}
1	0.72 1.42	1.0 6.4	0.58 3.7
2	0.22 0.89	-0.2 -1.3	0.36 2.3
7	0.14 0.52	0.69 5.1	0.46 3.4
5	0.58— —	—	—
6	0.70— —	—	—

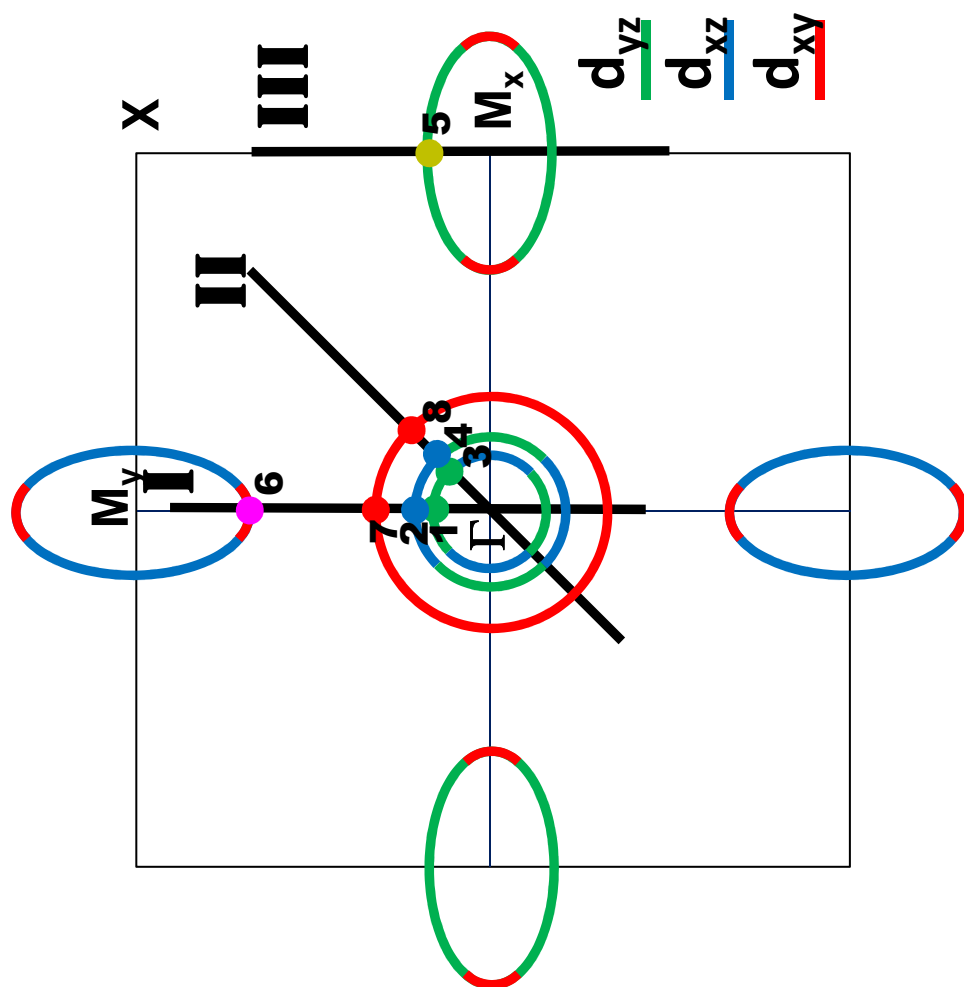


Figure 1

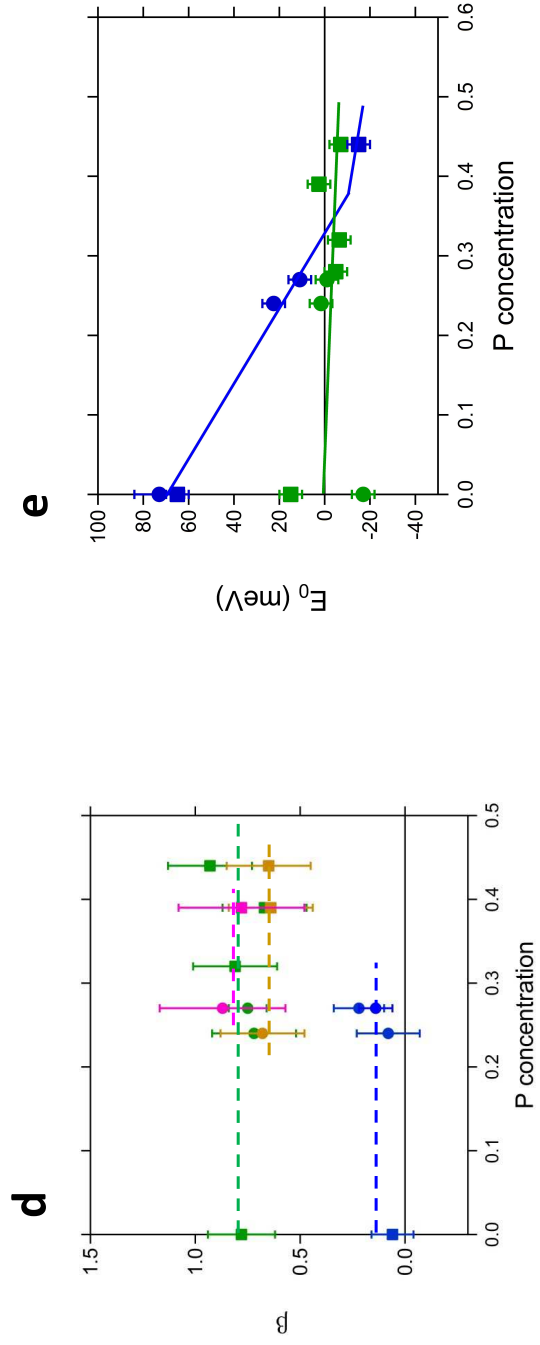
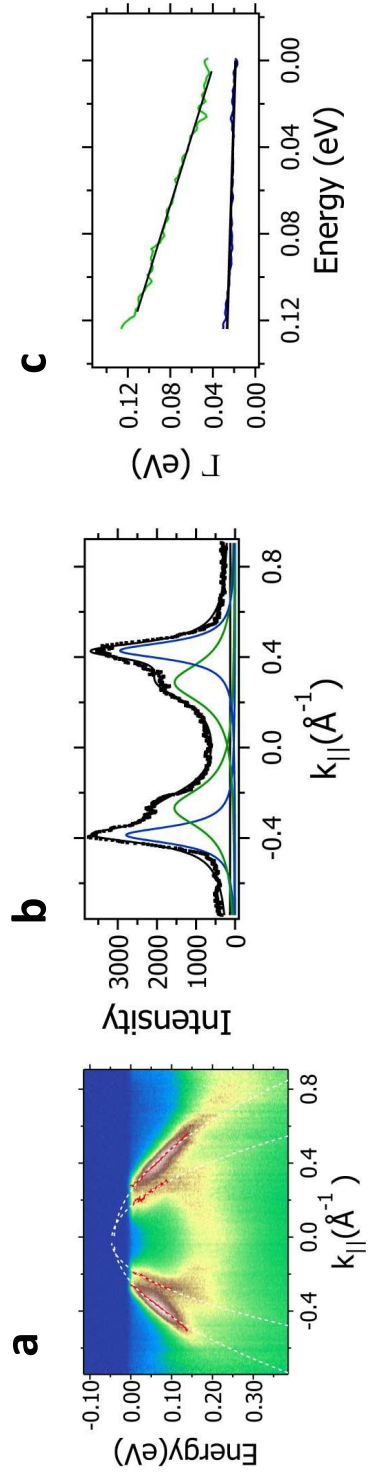


Figure 2

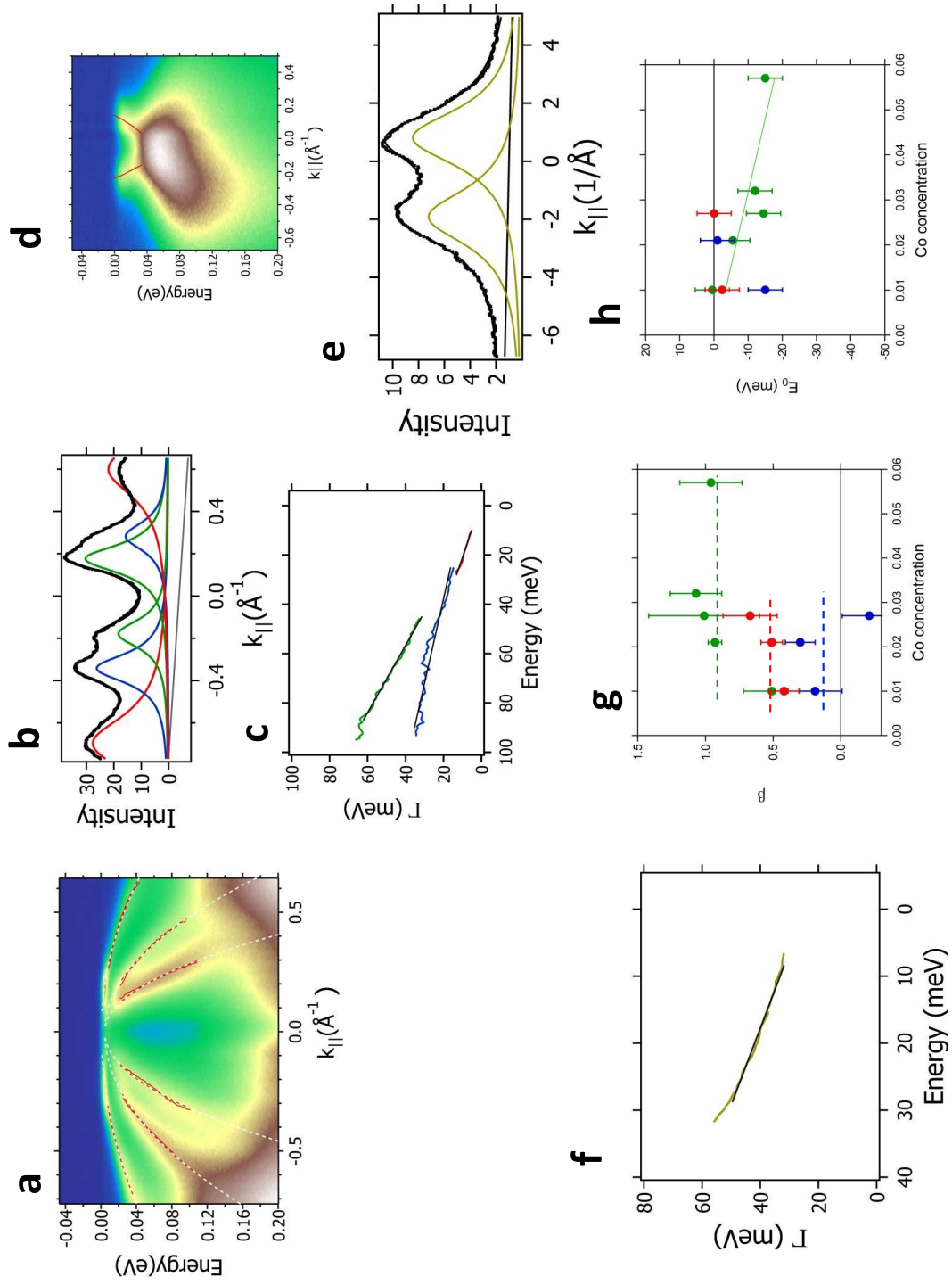


Figure 3

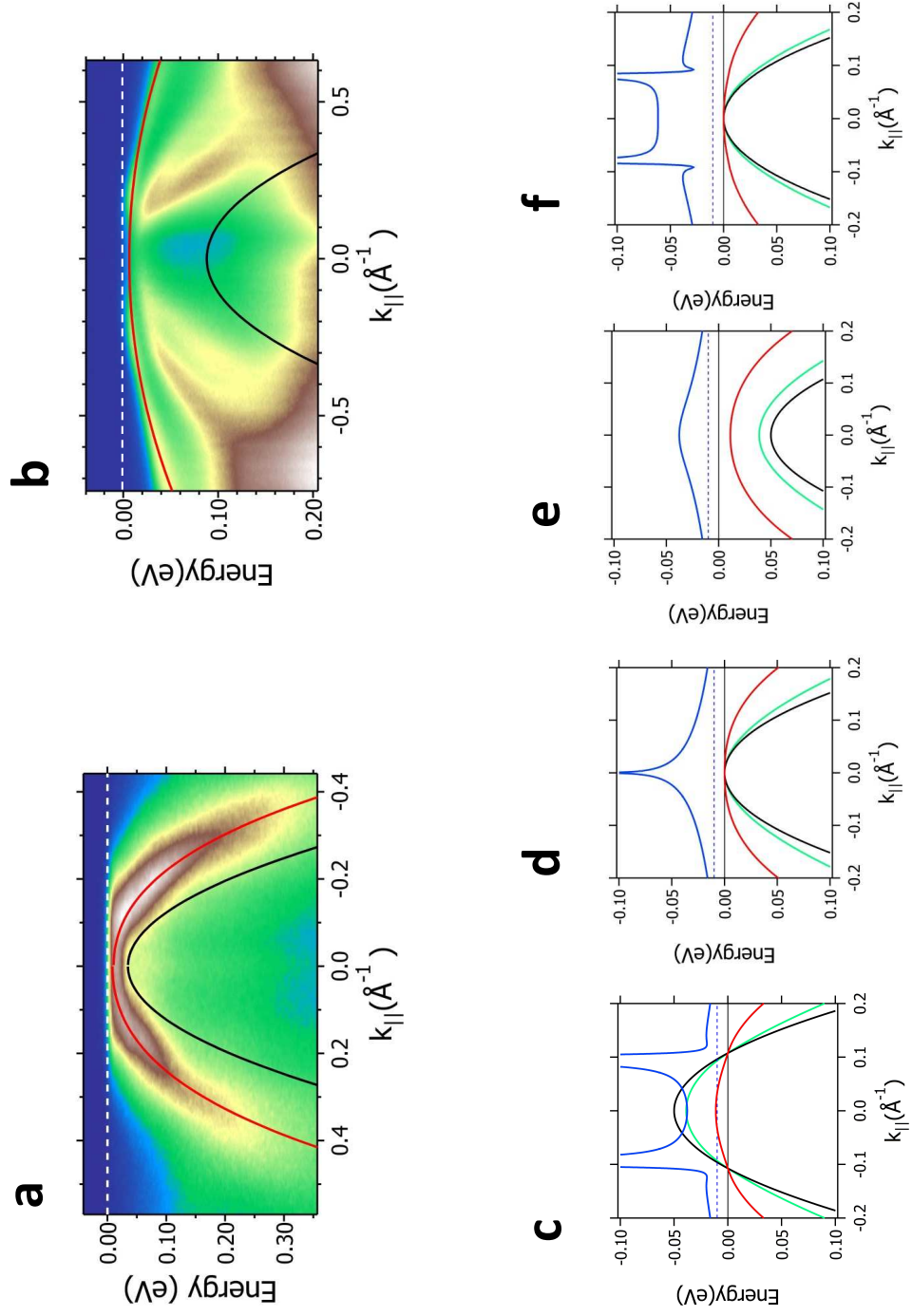


Figure 4

Figure 1 Fermi surfaces of ferropnictides. The Fermi surfaces in ferropnictides are formed by three hole pockets at Γ and electron pockets at M. Note that the back folded electron pockets are not shown, since the ARPES matrix elements are rather small. In case where part of the hole pockets have moved below the Fermi level, the figure shows constant energy plots at finite binding energies. The orbital character which was adopted from Ref.²³ is indicated by different colours. ARPES measurements were performed along three cuts, cut I, II, and III. In this way we could reach the points 1,2,7,3,4, and 8 on the hole pockets and the points 5 and 6 on the electron pockets.

Figure 2 ARPES data of $\text{BaFe}_2\text{As}_{2-x}\text{P}_x$ and $\text{EuFe}_2\text{As}_{2-x}\text{P}_x$. **a** Energy distribution map along cut I near Z of $\text{BaFe}_2\text{As}_{2-x}\text{P}_x$ $x=0.27$. **b** Momentum distribution curve taken from the data in **a** at a binding energy of 80 meV together with a fit using 4 Lorentzians related to the inner (green) and the middle (blue) hole pocket. **c** Scattering rates Γ as a function of binding energy for the inner (green) and the middle (blue) hole pocket together with a linear fit (black line). **d** compilation of all β values for various high symmetry points for $k_z = 0$ as a function of the P concentration. The colour code corresponds to that of the high symmetry points in Fig. 1. Circles and squares are data from $\text{BaFe}_2\text{As}_{2-x}\text{P}_x$ and $\text{EuFe}_2\text{As}_{2-x}\text{P}_x$, respectively. The horizontal dashed lines are guides to the eye. **e** Top of the inner (green) and the middle (blue) hole pocket as a function of the P concentration derived from a parabolic fit to the occupied part of the bands. Error bars in **d** and **e**: in case when several measurements were available for one P concentration, the error bar was calculated from the standard deviation. In case when only one measurement has

been performed, the error bar was estimated from the deviations detected in the first case by an extrapolation to a single measurement. Error bars in **e**: from the least squares fit.

Figure 3 ARPES data of $\text{NaFe}_{1-x}\text{Co}_x\text{As}$ and $\text{NaFe}_{1-x}\text{Rh}_x\text{As}$. **a** Energy distribution map along cut I near Γ of $\text{NaFe}_{1-x}\text{Rh}_x\text{As}$ $x=0.027$. **b** Momentum distribution curve taken from the data in **a** at a binding energy of 40 meV together with a fit using 6 Lorentzians related to the inner (green), the middle (blue), and the outer hole pocket (red). **c** Scattering rates Γ as a function of binding energy for the inner (green), the middle (blue), and the outer hole pocket (red) together with a linear fit (black). **d** Energy distribution map along cut III through the electron pocket. **e** Momentum distribution curve taken from the data in **d** at a binding energy of 20 meV together with a fit using 2 Lorentzians. **f** Energy dependence of the scattering rate Γ for the electron pocket at point 5. **g** compilation of all β values of $\text{NaFe}_{1-x}\text{Co}_x\text{As}$ for various high symmetry points for $k_z = 0$ together with a linear fit (black) as a function of the Co concentration. The colour code corresponds to that of the high symmetry points in Fig. 1. The horizontal dashed lines are guides to the eye. **h** Top of the inner (green) and the middle (blue) hole pocket as a function of the Co concentration derived from a parabolic fit to the occupied part of the bands. Error bars: see caption or Fig. 2.

Figure 4 Marginal Fermi liquid and mass enhancement . **a** Energy distribution map along cut I near Γ of $\text{BaFe}_2\text{As}_{2-x}\text{P}_x$ $x = 0.24$ together with a dispersion (red line) fitted to the data using a marginal Fermi liquid self-energy and a bare particle dispersion shown

by a black line. **b** Energy distribution map along cut I near Γ of $\text{NaFe}_{1-x}\text{Rh}_x\text{As}$ $x = 0.027$ together with a dispersion of the outer hole pocket (red line) fitted to the data using a marginal Fermi liquid self-energy and a bare particle dispersion shown by a black line. **c** Bare particle dispersion (black line) with parameters taken from DFT calculations of the inner hole pocket of BaFe_2As_2 with the top of the hole pocket 50 meV above the Fermi level together with calculations of $\Re\Sigma$ (green line) and the renormalized dispersion (red line) using the self-energy of a marginal Fermi-liquid with parameters derived from ARPES experiments. In addition we show the effective mass m^*/m_0 (blue line) and the $m^*/m_0 = 1$ line (thin dashed blue line). **d** The same as **c** but with the top of the hole pocket at the Fermi level. **e** The same as **c** but with the top of the hole pocket 50 meV below the Fermi level. **f** The same as **d** but with a self-energy having below 5 meV a Fermi-liquid behaviour.